

Liquid-liquid phase transition without the density anomaly

G. Franzese^{1,*}, G. Malescio², A. Skibinsky¹, S. V. Buldyrev¹, and H. E. Stanley¹

¹*Center for Polymer Studies and Department of Physics, Boston University, Boston, MA 02215, USA*

²*Dipartimento di Fisica, Università di Messina and Istituto Nazionale Fisica della Materia, 98166 Messina, Italy*

(Dated: May 21, 2019)

We present a detailed study in three dimensions of a single-component system interacting via an isotropic potential with an attractive well at intermediate distance and with a repulsive soft-core shoulder at short distance. By means of two independent numerical approaches, integral equations and molecular dynamics simulations, we show two lines of first order phase transitions. One separates gas and low-density liquid (LDL) and terminates in a critical point C_1 . The other separates at low temperature LDL and high-density liquid (HDL) but at high temperatures separates gas and HDL, and terminates in a second critical point C_2 . By the integral equation approach, we show that the energy and range of the repulsive soft-core play an essential role in determining the existence of the second critical point C_2 . By molecular dynamics simulations, we study the evolution of the liquid state showing its metastability with respect to the crystal phase. We relate the metastability with the small width of the attractive well. We study the structure of the phases and compare the results of the two different numerical approaches. Finally, we address the problem of the presence of the density anomaly. Phase diagrams with two fluid-fluid critical points have been presented in relation with the anomalous behavior of the density of network-forming fluids, including water, carbon, silicon and silica. We show here, by explicit thermodynamic calculation on the basis of our molecular dynamics results, that surprisingly our phase diagram with two critical points does not show the density anomaly. Since our potential is similar to potentials used to describe a variety of systems like liquid metals, protein solutions or colloids, our results raise the interesting possibility of the existence of a second critical point in these systems, independent of the presence of a density anomaly.

PACS numbers: 64.70.Ja, 61.20.Gy, 65.20.+w, 64.60.My

I. INTRODUCTION

Soft-core potentials have been widely used to study a variety of systems such as liquid metals, metallic mixtures, electrolytes and colloids, as well as anomalous liquids, like water and silica [1, 2, 3, 4, 5, 6, 7, 8, 9, 10, 11, 12]. In these models, the specific structural characteristic at the molecular (or atomic) level are neglected and the molecules (or atoms) are represented by simple spheres. Quantum effects (such as the quantum nature of chemical interactions) and classical effects (such as the Coulomb interaction) are modeled through a phenomenological isotropic pair potential. The advantages of this approach are that while these potentials are simple enough to be treated analytically [13], they still allow a qualitative comparison with the experiments. Moreover they can be studied by means of numerical simulations less time-consuming than those of realistic models [14].

Here we consider an off-lattice model in three dimensions (3D) [10] related to the soft-core potentials studied by Hemmer and Stell [2] for solid-solid critical points. Our model shows a phase diagram with two fluid-fluid phase transitions, a feature recently seen in experiments

on phosphorus [15] and confirmed by specific simulations [16]. The calculations in Ref. [10] show that both first-order fluid-fluid phase transitions end in critical points. For the considered potential, both transitions occur in the supercooled phase with respect to the crystal phase.

As an initial step of our study, we analyze the model with a fast numerical approach: the integral equation in the hyper-netted chain (HNC) approximation. This approach allows us to rationalize how, in addition to the low density critical point C_1 , the high density critical point C_2 arises as a function of the parameters of the pair potential. We then perform molecular dynamics (MD) simulations for a specific set of these parameters. We study the stable and metastable fluid phases, taking into consideration the finite size effect.

The study allows us to understand the relation of the critical point C_2 to the density anomaly. Since the hypothesis of a second critical point has been proposed [17] as a way to rationalize the density anomaly in network-forming fluids, like supercooled water [1, 17, 18], carbon [19, 20], silica [21, 22] and silicon [23], experimentalists have looked for a second critical point by focusing mainly on systems with the density anomaly [24, 25, 26, 27, 28] (Fig. 1a). Our MD study shows that the presence of the critical point C_2 does not necessarily induce the density anomaly, disclosing that the quest for simple liquids with two critical points is not restricted to systems with anomalous behavior in density (Fig. 1b).

This paper is organized as follows: in Section II, a brief introduction to soft-core potentials is given; in Sec-

*Present address: Dipartimento di Ingegneria dell'Informazione, Seconda Università di Napoli, INFN UdR Napoli and CG SUN, via Roma 29 I-81031, Aversa (CE), Italy, ; Electronic address: franzese@na.infn.it

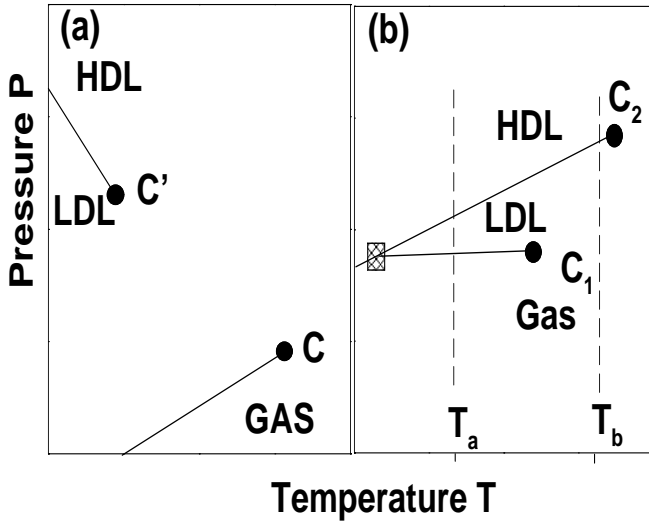


FIG. 1: Schematic pressure-temperature $P - T$ phase diagrams with two critical points. Solid lines represent first order phase transition lines, circles represent critical points. (a) Phase diagram with critical point C between the gas and the low-density liquid (LDL) at high T and low P and critical point C' between the LDL and the high-density liquid (HDL) at low T and high P . This phase diagram has been proposed for water. (b) Phase diagram with critical point C_1 between the gas and the LDL at low T and low P and critical point C_2 between the gas and the HDL at high T and high P . Increasing the pressure at constant temperature T_a below C_1 (dashed line at T_a), the system undergoes a first order phase transition between the gas and the LDL phases, followed by a first order phase transition between the LDL and the HDL phases. Increasing the pressure at constant temperature T_b above C_1 but below C_2 (dashed line at T_b), the system undergoes only a first order phase transition between the gas and the HDL. The square represents the gas-LDL-HDL triple point.

tion III, the HNC integral equation approach and results are described; in Section IV, the MD simulations are presented; in Section V, the HNC and MD results are compared; in Section VI the density anomaly issue is addressed. The summary and conclusions are given in Section VII.

II. SOFT-CORE POTENTIALS

Among the isotropic potentials, much attention has been devoted to soft-core potentials, which have a finite (soft-core) repulsion added to the infinite (hard-core) repulsion. The infinite repulsion is due to the impenetrability of the spheres. The finite repulsion represents the combination of all the quantum and classical repulsive effects averaged over the angular part. It has been shown [4] that such a weak effective repulsion can be derived by a first principle calculation for liquid metals [3]. To understand the possibility of the solid-solid critical point

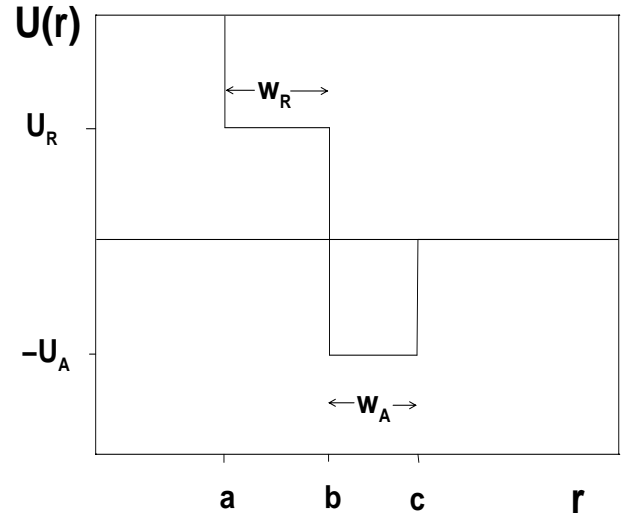


FIG. 2: The isotropic pairwise additive potential $U(r)$ as a function of the interparticle distance r : a is the hard-core distance, b is the soft-core distance, c is the cut-off distance, $-U_A < 0$ is the attractive energy and U_R is the repulsive energy. In this paper we consider both $U_R < 0$ and $U_R > 0$.

in material like Ce and Cs, Hemmer and Stell [2] proposed a soft-core potential with an attractive interaction at large distances, performing an exact analysis in 1D. Over the past thirty years, several other soft-core potentials with one or more attractive wells were proposed and studied with approximate methods, or numerical simulations in 2D, to rationalize the properties of liquid metals, alloys, electrolytes, colloids and the water anomalies [1, 2, 3, 4, 5, 6, 7, 8, 9, 10, 11, 12]. It has been recently shown [10], for the first time in 3D with MD, that an appropriate soft-core potential with an attractive well is able to show two supercooled liquids of different densities, with two critical points.

Following Ref. [10], we define the isotropic pair potential $U(r)$, as a function of the pair distance r (Fig.2):

$$U(r) = \begin{cases} \infty & \text{for } r < a \\ U_R & \text{for } a \leq r < b \\ -U_A & \text{for } b \leq r < c \\ 0 & \text{for } c \leq r \end{cases}, \quad (1)$$

where a is the hard-core distance and b is the soft-core distance. For $a \leq r < b$, the spheres interact with a finite (soft-core) repulsive energy U_R . For $b \leq r < c$, the pair's interaction is attractive with energy $-U_A < 0$. The distance c is the cut-off radius beyond which the pair's interaction is considered negligible. For sake of comparison with Ref. [9], we will consider both $U_R > 0$ and $U_R < 0$.

The step-like shape in Eq. (1) has the advantage of being defined by only three parameters: the width of the soft-core in units of the hard-core distance $w_R/a \equiv (b - a)/a$, the width of the attractive well in the same units $w_A/a \equiv (c - b)/a$ and the soft-core energy in units of

the attractive well energy U_R/U_A . To explore the phase diagram of the model as a function of these three parameters in an approximate, yet fast way, we use the integral equations in the HNC approximation.

III. THE INTEGRAL EQUATIONS IN THE HYPER-NETTED CHAIN APPROXIMATION

The radial distribution function $g(r)$ plays a central role in the physics of fluids [13]. This quantity is proportional to the probability of finding a particle at a distance r from a central one and can be written as

$$g(r) \equiv \frac{1}{N\rho^2} \left\langle \sum_i^N \sum_{j \neq i}^N \delta(\vec{r} + \vec{r}_j - \vec{r}_i) \right\rangle, \quad (2)$$

where \vec{r}_i is the position of particle i , $\delta(\vec{r})$ is the Dirac delta function, ρ is the density, supposed independent on r (uniform system), $\langle \dots \rangle$ denotes the average over different samples at the same temperature T and the sum is carried over to all the N particles in the system. The radial distribution function goes to 1 for large r and is always 1 for a random spatial distribution of particles. To represent deviations from randomness, the *total* pair correlation function $h(r) \equiv g(r) - 1$ is introduced. These functions are relevant because they are directly measurable by radiation scattering experiments and, provided that the particles interact through pairwise-additive forces, the thermodynamic properties of the fluid can be written with integrals over them. For example, the isothermal compressibility $K_T \equiv (\partial\rho/\partial P)_T/\rho$ can be measured as

$$k_B T \rho K_T = 1 + \rho \int h(\vec{r}) d\vec{r}, \quad (3)$$

where k_B is the Boltzmann constant.

The function $h(r)$ is the result of the interaction of all the particles of the system. Formally, $h(r)$ can be decomposed into the contribution coming from the *direct* interaction between two particle at distance r , called $c(r)$, and into the contribution due to the interaction propagated through any other particle in the system. The last contribution is written in turn as an integral convolution of direct correlations and total pair correlation.

This decomposition, for uniform systems, is expressed by the Ornstein-Zernike relation

$$h(r) = c(r) + \rho \int c(r') h(|\vec{r} - \vec{r}'|) d\vec{r}'. \quad (4)$$

The Eq. (4) is also the formal definition of $c(r)$. Both $h(r)$ and $c(r)$ in Eq. (4) are unknown functions, thus to solve this equation, one needs another relation (*closure*) between these two functions. This relation is provided by the diagrammatic expansion of $g(r)$ [13] which, after formal summation, yields the functional relation

$$g(r) = \exp[-\beta U(r) + h(r) - c(r) + d(r)], \quad (5)$$

where $U(r)$ is the interparticle potential, $\beta \equiv 1/(k_B T)$ and $d(r)$ is the sum over a specific class of diagrams [29]. Since $d(r)$ cannot be calculated exactly, one resorts to approximate expressions. The simplest approximation assumes $d(r) = 0$ (HNC closure) [30]. One expects this approximation to work better at lower ρ , where the direct correlation function $c(r)$ is more relevant than the correlation propagated through the other particles. However, our results (see Section V) will show that this intuitive observation is not straightforward, at least for soft-core potentials.

The solution of the integral Eqs. (4) and (5) with the HNC closure is obtained through a numerical iterative procedure whose essential scheme is the following. Under the assumption $d(r) = 0$, one can write $g(r)$ as

$$g(r) = \exp[-\beta U(r) + \theta(r)], \quad (6)$$

where the function $\theta(r) \equiv h(r) - c(r)$ is introduced due to its remarkable property of being a continuous function of r , even for discontinuous potentials (as in this paper). From the definitions of $h(r)$, $\theta(r)$ and Eq. (6), one can derive the equation

$$c(r) = \exp[-\beta U(r) + \theta(r)] - \theta(r) - 1. \quad (7)$$

By using the Fourier transform $\hat{f}(\vec{q}) \equiv \int f(\vec{r}) \exp(i\vec{q} \cdot \vec{r}) d\vec{r}$ defined for a generic function $f(\vec{r})$, from Eq. (4) we obtain

$$\hat{h}(q) = \hat{c}(q) + \rho \hat{c}(q) \hat{h}(q), \quad (8)$$

which gives

$$\hat{\theta}(q) = \rho \frac{\hat{c}^2(q)}{1 - \rho \hat{c}(q)} \quad (9)$$

with the $\theta(r)$ definition. The numerical iteration is based on Eqs. (7,9).

Starting with an initial guess for $\theta(r)$, we first calculate $c(r)$ by using Eq. (7). Its Fourier transform $\hat{c}(q)$ is used in Eq. (9) to calculate $\hat{\theta}(q)$. Its inverse Fourier transform provides a new $\theta(r)$ that is used as a new input for the next cycle. The elementary cycle is repeated until the output and input $\theta(r)$ differs less than the required accuracy.

Based on this iterative procedure, different algorithms can be used to improve the accuracy and rapidity of convergence of the numerical solution of HNC equations. However, independently of the algorithm used, there exists a region in the ρ - T plane where no solution can be found, i.e. for any ρ , there is a T below which the numerical algorithm does not converge, defining an ‘instability line’ in the ρ - T plane.

It has been observed that for a large number of simple fluid pair potentials, the shape of the instability line qualitatively resembles the region of spinodal decomposition of the fluid [31]. However, a strict identification of the instability line with the spinodal line of the fluid is not possible. In fact, approaching the spinodal line

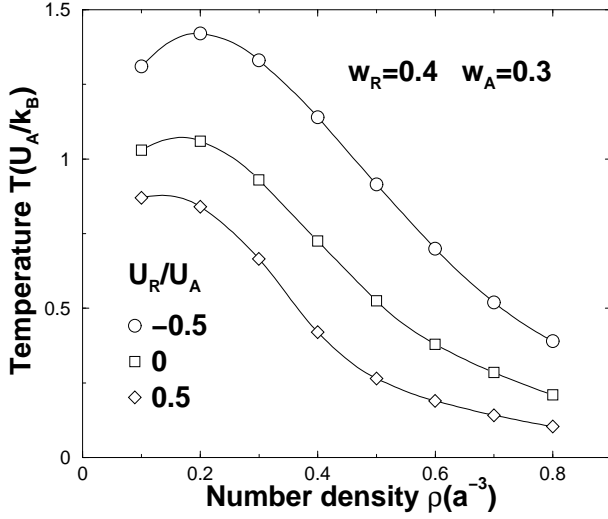


FIG. 3: Instability line of the HNC equations in 3D in the ρ - T plane for the pair potential in Eq. (1), with $w_R = 0.4$, $w_A = 0.3$ and (from top to bottom) $U_R/U_A = -0.5, 0, 0.5$. For $U_R/U_A = -0.5$, the pair potential recovers the one studied in 1D and 2D in Ref. [9]. The symbols represent the calculations and the lines are guides for the eyes.

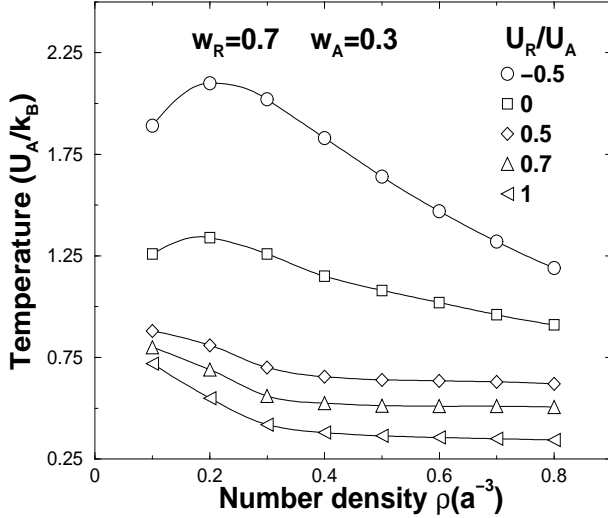


FIG. 4: Instability lines, as in Fig. 3, for the pair potentials with parameters $w_R = 0.7$, $w_A = 0.3$ and (from top to bottom) $U_R/U_A = -0.5, 0, 0.5, 0.7, 1$.

by decreasing T at constant ρ , the isothermal compressibility K_T diverges, while the HNC equations predict a diverging K_T only in some particular ρ - T regimes [32]. Nevertheless, as shown by comparison with the MD results (Section V), the HNC instability line is qualitatively consistent with the spinodal line [33].

First, we calculate the instability line of the HNC equation for the potential investigated in Ref. [9]. The corresponding parameters are $w_R = 0.4$, $w_A = 0.3$ and $U_R/U_A = -0.5$. In this case, the soft-core is given by

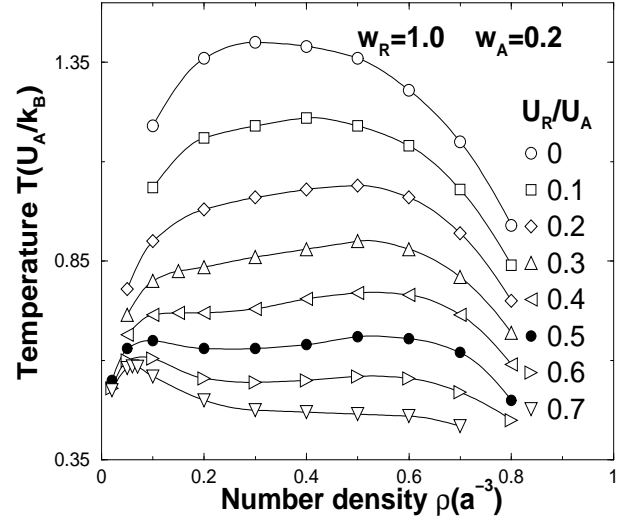


FIG. 5: Instability lines, as in Fig. 3, for the pair potentials with parameters $w_R = 1$, $w_A = 0.2$ and (from top to bottom) $U_R/U_A = 0, 0.1, 0.2, 0.3, 0.4, 0.5, 0.6, 0.7$. The full symbols correspond to the set of parameters selected for the MD calculations.

two attractive wells with different depths. Calculations in 1D and 2D [9] have shown a liquid-like density anomaly. Therefore, it is interesting to analyze the phase diagram in 3D. However, the instability line for this case (see Fig. 3) is similar to the spinodal line usually exhibited by a simple fluid, e.g. interacting via a Lennard-Jones potential with the maximum of the spinodal line corresponding to the liquid-gas critical point. Upon increasing U_R/U_A to 0.5 (Fig. 3), the only evident change of the instability line is a shift toward a lower T as a result of the overall decrease of the interparticle attraction, with no hints of a second critical point. A small shift to lower ρ is also seen. This behavior is more evident for larger w_R .

Next, we consider a potential with a larger w_R ($w_R = 0.7$, $w_A = 0.3$). The instability line is calculated for several values of U_R/U_A (Fig. 4). Upon increasing U_R/U_A , we now find not only the shift to a lower T , but also an evident shift of the maximum of the line (i.e. the critical point, if the instability line is identified with the spinodal line) to a lower ρ . This result can be rationalized by observing that, as U_R/U_A increases, the soft-core becomes more and more difficult to penetrate and for U_R/U_A large enough, the fluid behaves as a system of hard spheres with a diameter b interacting through an attractive well of width $c - b$ and energy $-U_A$. Consequently, the critical point's density moves to the value $\rho_c \approx \rho_{HS}(a/b)^3 < \rho_{HS}$, where ρ_{HS} is the critical point's density for a fluid of hard spheres with a diameter a interacting through an attractive well of width $c - a$ and energy $-U_A$. Since $c - b < c - a$, the overall attraction decreases for increasing U_R/U_A and, as a result the maximum of the instability line moves to a lower T .

Comparing Fig. 3 and Fig. 4, we note an important dif-

ference. In the case of a larger w_R , as U_R/U_A increases, the temperature of the instability line does not decrease for increasing ρ , but becomes rather flat. This result suggests that a marked change in the instability line might be observed for a potential with an even larger w_R .

We thus consider a potential with $w_R = 1$ and $w_A = 0.2$. The results (Fig. 5) show that for $0.4 \leq U_R/U_A \leq 0.6$, the instability line has two well-distinct local maxima, suggesting the possibility of two critical points in the phase diagram for the fluid phases [34]. For $U_R/U_A \leq 0.3$ or $U_R/U_A \geq 0.7$, the instability line shows just one maximum, similar to the typical spinodal line of a fluid of hard spheres with diameter a or b , respectively. As a consequence of this analysis, we choose $w_R = 1$, $w_A = 0.2$ and $U_R/U_A = 0.5$ as the set of parameters for the potential used in the MD calculations in 3D [10].

IV. THE MOLECULAR DYNAMICS APPROACH

We perform MD simulations with a constant number of particles N of unit mass m , a constant volume V and a constant average temperature T . We present the results for $N = 490$ and $N = 1728$. The average temperature is set by coupling the system to a thermal bath at the assigned T , with a thermal exchange coefficient per particle between the system and the bath equal to $k = 0.015 (U_A/m)^{1/2} k_B/a$. We use a standard collision event list algorithm [35] to evolve the system and a modified Berendsen method to achieve the desired T [36].

The pressure is calculated by using the virial expression for a step potential [14]

$$P = \frac{m}{3V} \left\langle \sum_i v_i^2 + \frac{1}{\Delta t} \sum_{i,j} \Delta \vec{v}_i \cdot (\vec{r}_i - \vec{r}_j) \right\rangle, \quad (10)$$

with $\sum_{i,j}$ sum over of the particles pairs (i,j) undergoing a collision in the time interval $\Delta t (ma^2/U_A)^{-1/2} = 10^{5/2}$ and with $\Delta \vec{v}_i \equiv \vec{v}'_i - \vec{v}_i$, where \vec{v}_i and \vec{v}'_i are the velocities of the particle i at position \vec{r}_i before and after the collision with the particle j at position \vec{r}_j , respectively.

First, we locate the equilibrium crystal line (Fig. 6) by simulating the system prepared in a configuration with 90% of the particles in a crystal seed surrounded by the fluid phase. We define the system to be in the solid phase if, after a time $10^6 (ma^2/U_A)^{1/2}$, the crystal seed is growing and we consider it in a fluid phase if the seed is melting. The cases in which the trend is not clear within the simulation time are considered as belonging to the first-order transition region [37]. The crystallization pressure rapidly increases with ρ and T , giving a first-order transition line (in the thermodynamic limit) that separates the equilibrium P - ρ phase diagram in a high- T fluid and a low- T crystal (Fig. 6).

At equilibrium, there is no (stable) liquid phase. However, the liquid is present as a metastable (supercooled)

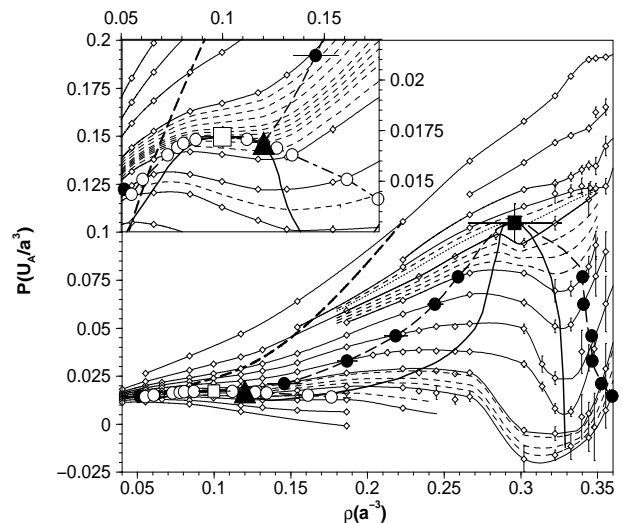


FIG. 6: The MD phase diagram in the pressure-density plane. The diamonds are MD calculations for temperatures (bottom to top) $k_B T/U_A = 0.570, 0.580, 0.590, 0.595, 0.600, 0.610, 0.620, 0.630, 0.640, 0.650, 0.660, 0.670, 0.680, 0.690, 0.700$. The solid lines connecting the diamonds are interpolations of the calculations at constant T (isotherms). The dashed lines are linear interpolations between isotherms. The thick long dashed line is the fluid-crystal first-order transition line. The solid thick line connecting the local minima and maxima along the isotherms is the spinodal line. The full circles, connected by the long dashed line, define the border of the gas-HDL coexistence region. The open circles, connected by the dot-dashed line, define the border of the gas-LDL coexistence region (enlarged view in the inset). The low-density gas-LDL critical point C_1 and the high-density gas-HDL critical point C_2 are indicated by an open and a full squares symbol, respectively. The full triangle is the estimate of the triple (gas-LDL-HDL) point. Where not shown, the errors are smaller than the symbols.

phase with respect to the crystal phase. To study the metastable phase diagram, we equilibrate the system for each ρ from a high T configuration at $k_B T/U_A = 0.70$ and then rapidly cool it to the desired T , calculating the energy U , pressure P , radial distribution function $g(r)$ and structure factor $S(q)$ for temperatures $k_B T/U_A \geq 0.57$.

Our calculations show that the supercooled fluid phase has a life-time longer than $10^6 (ma^2/U_A)^{1/2}$ (the standard length of our simulations) for densities $\rho \lesssim 0.20/a^3$ for $T \approx 0.57 U_A/k_B$, $\rho \lesssim 0.27/a^3$ for $T \approx 0.65 U_A/k_B$ and $\rho \lesssim 0.34/a^3$ for $T \approx 0.70 U_A/k_B$. After a time $6 \times 10^3 (ma^2/U_A)^{1/2}$, on average, the system is equilibrated in the fluid phase. We therefore discard the configurations in the time-interval $0 - 6 \times 10^3 (ma^2/U_A)^{1/2}$ and average each state point over the configurations in the time-interval $10^5 (ma^2/U_A)^{1/2} - 10^6 (ma^2/U_A)^{1/2}$ after binning the data within the same MD step Δt .

At a larger ρ , the system spontaneously crystallizes (homogeneous nucleation process). Thus, we only aver-

age configurations occurring before the nucleation. To be sure that our estimates are carried out in the fluid phase, we study the time evolution of the structure factor, which can be written as

$$S(\vec{q}, t) \equiv \frac{1}{N} \left\langle \sum_{j=1}^N \sum_{l=1}^N e^{i\vec{q} \cdot [\vec{r}_j(t) - \vec{r}_l(t)]} \right\rangle, \quad (11)$$

where $\vec{r}_j(t)$ is the position of particle j at time t . At equilibrium, $S(\vec{q}, t)$ averaged over the time and the wave vectors with the same module, gives the static structure factor $S(q) \equiv 1 + \rho \hat{g}(q)$, describing the spatial correlation in the system. Therefore, $S(\vec{q}, t)$ is related to the time-evolution of the spatial correlation and is $S(\vec{q}, t) \sim O(1)$ for a fluid-like configuration for all \vec{q} . For a crystal-like configuration, there is at least one wave vector such that $S(\vec{q}, t) \sim O(N)$.

The time-evolution of $S(\vec{q}, t)$ for a typical simulation inside the nucleation region is presented in Fig. 7. To limit the computational effort, we consider 9×10^4 wave vectors with modulus $q \leq 100 \text{ a}^{-1}$ much larger than the largest peak of the crystal structure factor at $q \approx 12.5 \text{ a}^{-1}$ (Fig. 7c). Three different regimes can be distinguished in the example in Fig. 7.

- (i) A short-time regime “A”, in which $S(\vec{q}, t) \sim O(1)$ for any q ($q = 1 \text{ a}^{-1}$ and $q \approx 12 \text{ a}^{-1}$ are shown in Fig. 7a, b). Averaged on this interval (curve A in Fig. 7c) the $S(q)$ is fluid-like.
- (ii) An intermediate-time regime “B”, in which $S(\vec{q}, t)$ for $q = 1 \text{ a}^{-1}$ has an increase, but has no increase for $q \approx 12 \text{ a}^{-1}$. Averaged on this interval (curve B in Fig. 7c) the $S(q)$ is fluid-like, but with an increase for $q \rightarrow 0$ that, according to the equation

$$k_B T \rho K_T = \lim_{q \rightarrow 0} \chi(q), \quad (12)$$

indicates an increase of K_T , associated with the phase separation into two fluids with different densities. To help visualize the phase separation, in Fig. 8 we show the three planar projections of the 3D snapshot corresponding to the largest peak in the time-interval “B” for $q = 1 \text{ a}^{-1}$ (Fig. 7a). By dividing the box into two equal parts, the histograms of the number of particles in each part (Fig. 8) show a separation in density approximately at half box-length, corresponding to $q = 4\pi(\rho/N)^{1/3} \approx 1 \text{ a}^{-1}$ for $\rho = 0.27 \text{ a}^{-3}$ and $N = 490$, in agreement with the peak in Fig. 7a. In each projection, it is possible to see regions of high density and low density.

- (iii) A long-time regime “C”, in which is $S(\vec{q}, t) \sim O(N)$ for $q \approx 12 \text{ a}^{-1}$, revealing the crystal nucleation process. The $S(q)$ averaged over this time interval (curve C in Fig. 7c) is solid-like. In the same interval, $S(\vec{q}, t)$ for $q = 1 \text{ a}^{-1}$ has a large increase, corresponding to the increases of K_T ($S(q)$ increases

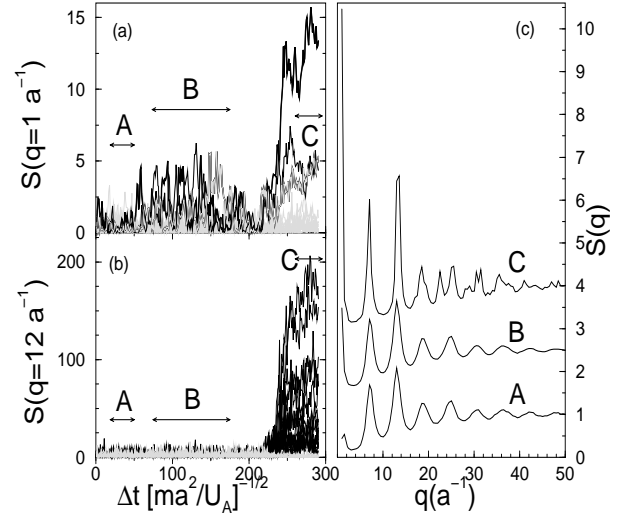


FIG. 7: MD calculations. (a) Time evolution of the structure factor $S(\vec{q}, t)$ at $T = 0.62 U_A / k_B$ and $\rho = 0.27 \text{ a}^{-3}$, for wave vectors with $q \approx 1 \text{ a}^{-1}$ and for a time $300 \Delta t (ma^2 / U_A)^{1/2}$ expressed in dimensionless units $\Delta t (ma^2 / U_A)^{1/2} = 10^{5/2}$; in the time-interval $[20, 50] \Delta t (ma^2 / U_A)^{1/2}$, labeled with “A”, for all the wave vectors the structure factor is $\sim O(1)$; in the time-interval “B”, $[70, 180] \Delta t (ma^2 / U_A)^{1/2}$, for six wave vectors there is a small increase in the structure factor; in the interval “C”, $[210, 300] \Delta t (ma^2 / U_A)^{1/2}$, for the same six wave-vectors there is a larger increase. (b) As in (a) but for $q \approx 12 \text{ a}^{-1}$; in this case there is a large increase in the structure factor only in the time interval “C”, more than one order of magnitude, for several wave vectors, showing in a clear way the formation of a crystal seed. (c) The averages over the time-intervals “A”, “B” and “C” of the structure factor $S(q)$, averaged over the wave vectors with the same modulus. The curves for “B” and “C” are shifted up of 1.5 and 3, respectively, for sake of clarity. All the curves go to 1 for large q . In the interval “A”, $S(q)$ is liquid-like. In the interval “B”, $S(q)$ is still liquid-like but with an increase for $q \rightarrow 0$, while in the interval “C” is solid-like, with two large peaks at $q \approx 7 \text{ a}^{-1}$ and $q \approx 12.5 \text{ a}^{-1}$ and a large value for $q \rightarrow 0$.

for $q \rightarrow 0$), which is consistent with the phase separation between the fluid and the crystal. As an example, in Fig. 9 we show the last snapshot of the time series in Fig. 7, where a crystal structure is clearly seen.

The example in Fig. 7 shows the formation of a high density fluid phase within the time interval “B”, followed by the nucleation of the crystal phase. The onset of the nucleation is marked by a large increase of $S(\vec{q}, t)$ for all the wave vectors corresponding to the peaks in the crystal $S(q)$ and by a large step-like decrease of energy. By repeating this analysis for all the calculations inside the region with nucleation, it is possible to calculate the state points corresponding to the metastable fluid phase. The phase diagram in Fig. 6 is based on averages over a total of $10^5 - 10^6$ configurations in the fluid phase,

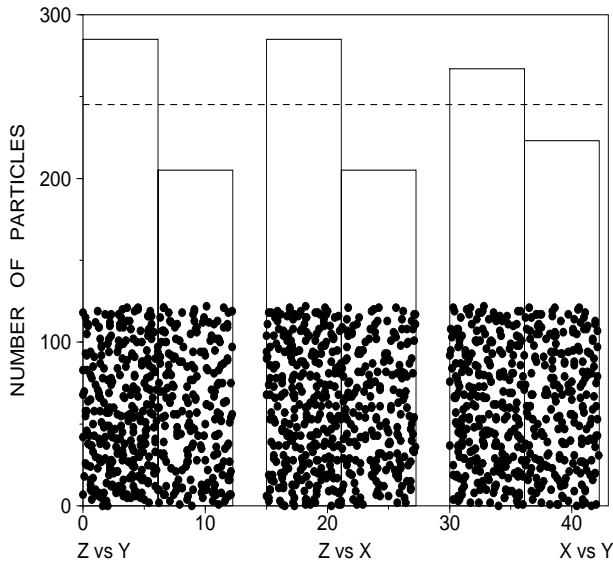


FIG. 8: Projections of the 3D snapshots corresponding to the largest peak in the time interval B in Fig. 7a. The projections are (from left to right) Z vs Y, Z vs X and X vs Y. The histograms of number of particles as functions of the abscissa is overimposed on each projection. Projections and histograms are shifted for the sake of clarity. Each histogram bin corresponds to half of the box. The dashed line shows the average number of particles in each bin for a uniform configuration ($N/2 = 245$). The largest deviation from the average is $40 > \sqrt{N} \approx 22$, i.e. twice the statistic fluctuation for a random distribution of particles.

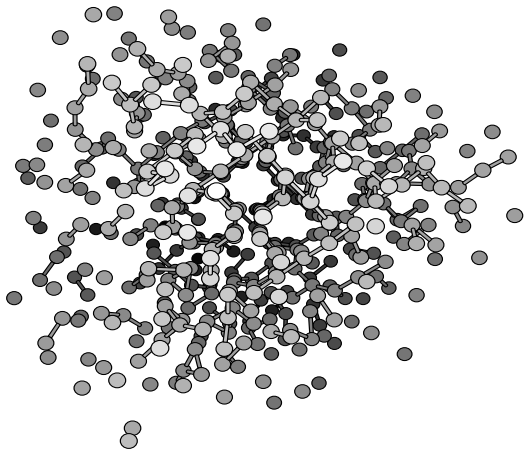


FIG. 9: MD snapshots of the last configuration in the time series in Fig. 5. A crystal nucleus surrounded by gas is clearly seen. For sake of clarity, we plot the spheres with diameter $a/2$. Bonds connect particles at distance $r \leq 1.1a$. A gray scale is used to give the perspective (darker spheres are at larger distance from the viewpoint).

accumulated in independent runs.

At low T (for $T \lesssim 0.67U_A/k_B$), the isotherms in Fig. 6 have a non-monotonic behavior at high ρ . A region where P decreases for increasing ρ is mechanically unstable and indicates the separation of the (fluid) system into two coexisting phases, characterized by different densities. By definition, these phases are gas and high-density liquid (HDL).

At lower T (for $T \lesssim 0.61U_A/k_B$), the isotherms are non-monotonic at both low ρ and high ρ (inset in Fig. 6). By definition, the coexisting phases are gas and low-density liquid (LDL).

By using the Maxwell construction of the equal areas for the non-monotonic isotherms in the P - V phase diagram [1], it is possible to estimate the two coexistence regions at low and high ρ . The point where the gas-LDL coexistence region merges with the extrapolation of the gas-HDL coexistence region is the estimate of the (gas-LDL-HDL) triple point (see the inset).

Inside each coexistence region, the locus of local maxima and minima along the isotherms defines the spinodal line. This line represents the limit of (mechanical) stability of each of the coexisting phases. In the low- ρ coexistence region, the maxima along the isotherms represent the limit of stability of the gas phase and the minima represent the LDL limit of stability. In the high- ρ coexistence region, the maxima represent the limit of stability for the gas at $T > 0.605U_A/k_B$ and the limit of stability for the LDL at $T \leq 0.605U_A/k_B$. The minima are the HDL limit of stability.

The points where the spinodal line meets the vertices of the two coexistence lines locate the two critical points. The estimates are, for the gas-LDL critical point C_1 , $k_B T_1/U_A = 0.605 \pm 0.004$, $a^3 \rho_1 = 0.10 \pm 0.01$, $a^3 P_1/U_A = 0.0170 \pm 0.005$ and, for the gas-HDL critical point C_2 , $k_B T_2/U_A = 0.665 \pm 0.005$, $a^3 \rho_2 = 0.295 \pm 0.030$ and $a^3 P_1/U_A = 0.105 \pm 0.010$. These values are consistent with the linear interpolations of the MD isotherms (Fig. 6) [38].

The metastability of the critical points is consistent with previous results [39] for a generalized Lennard-Jones (LJ) potential with an attractive well smaller than the standard LJ potential. For an attractive well with width less than $1/3$ of the hard-core, the generalized LJ potential has a critical point that is metastable with respect to the crystal [40]. In our case, the ratio is $w_A/a = 0.2 < 1/3$. Preliminary calculations for the potential studied here but with a well width larger than $1/3$ show that both critical points are stable with respect to the crystal.

Note that the phase diagram resulting from the MD calculations is, as expected, consistent with the time-dependent analysis of the structure factor presented above. For example, the case presented in Fig. 7 corresponds to a state point inside the gas-HDL coexistence region at a density higher than the crystal nucleation density for $T = 0.62U_A/k_B$. The nucleation of the (metastable) HDL phase is thus followed by the crystal

nucleation.

To estimate the finite size effect on our calculations, we compare the results for $N = 490$ and $N = 1728$ (Fig. 10) for an isotherm below both critical points. The calculations do not show any relevant finite size effect, suggesting that the MD calculations for $N = 490$ are reliable.

V. COMPARISON BETWEEN THE HYPER-NETTED CHAIN APPROXIMATION AND THE MOLECULAR DYNAMICS RESULTS

From these results, we can see that the interpretation of the HNC instability line is qualitatively consistent with the MD spinodal line for the corresponding set of the potential's parameters. The projection of the MD spinodal line in the T - ρ plane (not shown) has the same characteristics of the HNC instability line, with two local maxima and one local minimum. In both approaches, the high- ρ local maximum occurs at a temperature higher than the temperature of the low- ρ maximum and the presence of a triple point is suggested by the presence of the local minimum.

The quantitative HNC predictions for the locations of the two critical points are, as expected, partially consistent with the MD results. It is remarkable that the HNC estimates of the density of the critical point C_1 ($\rho \approx 1a^{-3}$) and the temperature of the critical point C_2 ($T \approx 0.65U_A/k_B$) are close to the MD estimates.

The HNC approximation is expected to be worse in the vicinity of a critical point or at high density. However, at intermediate ρ , the consistency of our calculations for the $g(r)$, in both HNC and MD approaches, is larger than at low ρ (Fig. 11), showing that the HNC underestimates the probability of a particle penetrating the soft-core and entering the attractive well when the density is low.

The $g(r)$ of the low- ρ fluid is characterized by a large peak at $r = b$, i.e., in correspondence of the soft-core distance. Increasing the density, the peak at $r = a$ increases while the peak at $r = b$ decreases, and additional peaks at $r/a = 3, 4, \dots$ appear (Fig. 12). From the definition of the mean number of particles at a distance between r and $r + dr$ from a reference particle,

$$n(r)dr = 4\pi r^2 \rho g(r)dr, \quad (13)$$

by using the MD $g(r)$, we calculate the average number of particles $N(r) = \int n(r)dr$ within a sphere of radius r (Fig. 13), observing, for increasing ρ , a moderate increase of particles within the repulsive range and a large increase within the attractive range.

VI. ABSENCE OF A DENSITY ANOMALY

The low temperature behavior of liquid water and other network-forming liquids like silica, is characterized by thermodynamic anomalies. By cooling at constant P ,

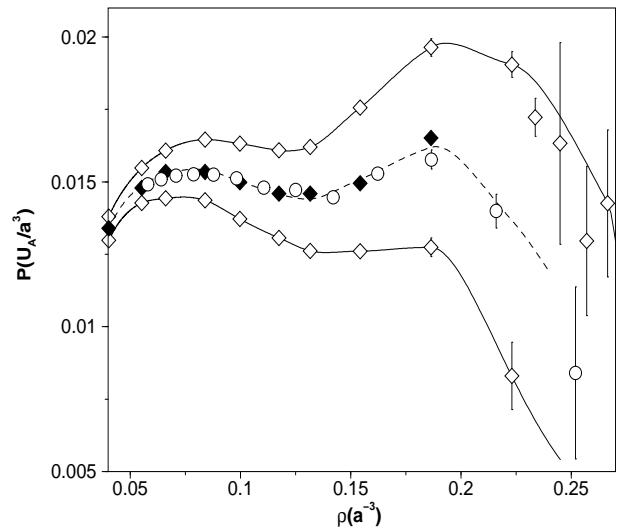


FIG. 10: Comparison between MD simulations for $N = 490$ (diamonds) and $N = 1728$ (circles) at $k_B T/U_A = 0.595$. The results for the two sizes are very close, both showing the presence of two regions with negatively sloped isotherms. For comparison, we include also the calculations for $N = 490$ at $k_B T/U_A = 0.60$ and 0.59 (upper open diamonds and lower open diamonds, respectively) and the interpolation at $k_B T/U_A = 0.595$ (dashed line) between these two isotherms. The points calculated for $N = 1728$ are also consistent with this interpolation, suggesting that the finite size effect between $N = 490$ and $N = 1728$ is small. Errors, where not shown, are smaller than the symbols.

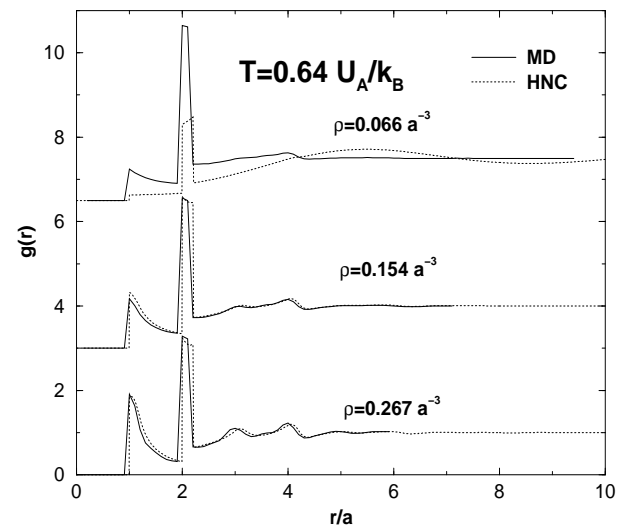


FIG. 11: Comparison between the $g(r)$ calculated by HNC (dotted line) and by MD (solid line). As an example, we present the calculations at $T = 0.64U_A/k_B$ for densities (from top to bottom) $\rho a^3 = 0.066, 0.154, 0.267$. For sake of clarity a constant value is added to the first two curves (6.4 and 3, respectively). As shown, the two independent calculations are very close at intermediate densities. At large r all the curves go to 1.

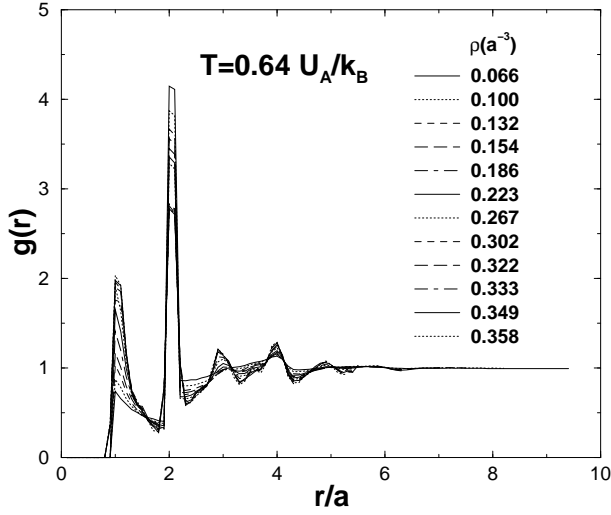


FIG. 12: The MD $g(r)$ at $T = 0.64U_A/k_B$ for densities $\rho/a^{-3} = 0.066, 0.100, 0.132, 0.154, 0.186, 0.223, 0.267, 0.302, 0.322, 0.333, 0.349, 0.358$. With increasing ρ , the peak at $r = a$ increases and the peak at $r = b$ decreases, while more peaks appear at larger r .

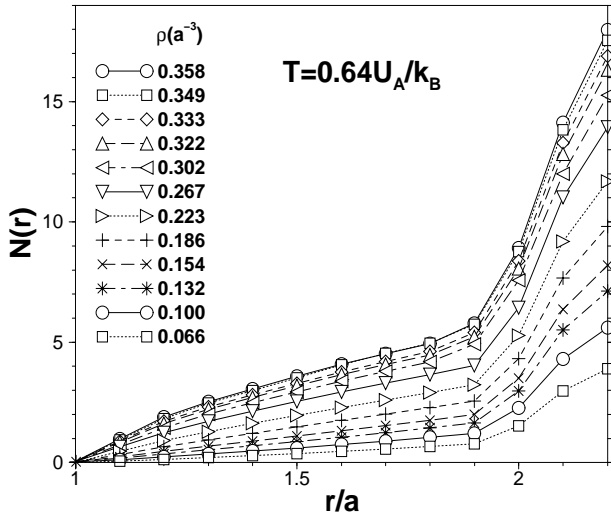


FIG. 13: The MD $N(r)$ at $T = 0.64U_A/k_B$ for the densities in Fig. 12 for $a \leq r \leq c$ (with $b/a = 2$ and $c/a = 2.2$). With increasing ρ , the cumulative number of particles within the interaction range c increases from 4 to 18.

the density decreases below a temperature T_{MD} of maximum density instead of increasing as in normal liquids and the response functions (specific heat at constant pressure, isobaric compressibility and absolute value of thermal expansion coefficient) increase, instead of decreasing [1].

Poole et al. [17] have proposed, on the basis of MD simulations for a realistic model potential for water, a rationalization of these anomalies as consequence of the presence of a liquid-liquid critical point in the supercooled

phase. Many experimental [24, 25, 26, 27, 28] and theoretical [1, 9, 11, 12, 17, 18, 19, 20, 21, 22, 23, 41, 42] studies have been focused on water and other liquids with anomalous density to uncover the presence of a second critical point. We show here that the possibility of a second fluid-fluid critical point is not necessarily restricted to systems with a density anomaly, at least from a theoretical point of view.

The defining relation for the density anomaly is given by

$$\left. \frac{\partial V}{\partial T} \right|_P < 0. \quad (14)$$

From the Maxwell relations, we know that

$$\left. \frac{\partial V}{\partial T} \right|_P = - \left. \frac{\partial S}{\partial P} \right|_T, \quad (15)$$

where S is the entropy. Since

$$\left. \frac{\partial V}{\partial P} \right|_T < 0 \quad (16)$$

holds for a mechanically stable phase, Eq. (14) can be rewritten as

$$\left. \frac{\partial S}{\partial V} \right|_T \left. \frac{\partial V}{\partial P} \right|_T > 0, \quad (17)$$

or

$$\left. \frac{\partial S}{\partial V} \right|_T < 0. \quad (18)$$

From the differential expression of the thermodynamic potential at constant T , we know that

$$TdS = dU + PdV, \quad (19)$$

where U is the total potential energy. Therefore, it is

$$\left. \frac{\partial S}{\partial V} \right|_T = \frac{1}{T} \left. \frac{\partial U}{\partial V} \right|_T + \frac{P(V, T)}{T} \quad (20)$$

at constant T and we can rewrite the density anomaly condition in Eq. (18) as

$$\left. \frac{\partial U}{\partial V} \right|_T + P(V, T) < 0 \quad (21)$$

at constant T .

To calculate the left-hand side of Eq. (21), we need to evaluate $(\partial U/\partial V)_T$. In Fig. 14, we show our MD calculation for $U(\rho)$ at constant T . All the MD points can be fitted with a third degree polynomial in ρ . The fitting parameters are given in Table I and are used to calculate the derivative $(\partial U/\partial V)_T$. Our calculations show a potential energy U increasing with V (inset Fig. 15), with a derivative always positive (Fig. 15), thus wherever P is positive, the condition in Eq. (21) is not satisfied and there is no density anomaly.

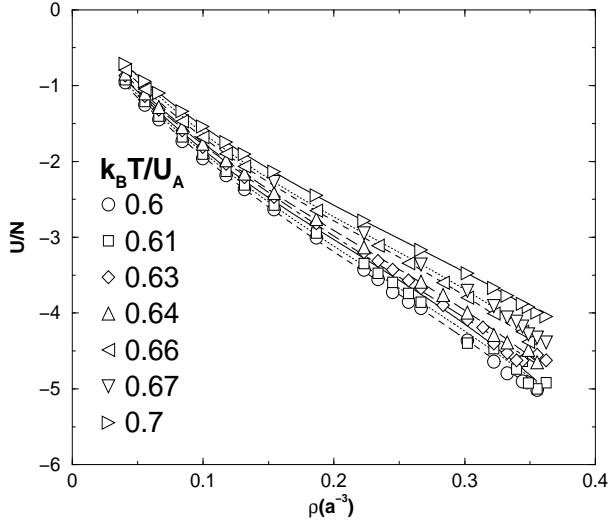


FIG. 14: The MD energy density U/N as a function of the density ρ for temperatures (bottom to top) $k_B T/U_A = 0.6, 0.61, 0.63, 0.64, 0.66, 0.67, 0.7$. The symbols represent the MD calculations, with errors smaller than the symbol's size. The lines represent the cubic fit of the calculations with the parameters in Tab. I.

In the region where $P < 0$ (at small V), the derivative $(\partial U/\partial V)_T$ rapidly increases in such a way that Eq. (21) is never satisfied. Particularly, in the range of volumes considered, it is always $(\partial U/\partial V)_T - 0.025U_A/a^3 > 0$, where $P = -0.025U_A/a^3$ is the minimum pressure, reached for $T = 0.6U_A/k_B$ and $V/N = 3.31a^3$.

VII. SUMMARY AND CONCLUSIONS

We have presented the study of a soft-core potential with a phase diagram showing two fluid-fluid phase transitions by means of two independent numerical methods: (i) integral equations in the HNC approximation and (ii) MD simulations.

By comparing the HNC results with previously-proposed soft-core potentials, we conclude that the energy and the width of the repulsive soft-core play an essential role in the presence of the second critical point C_2 . We select a set of potential parameters with a narrow attractive well that gives a HNC instability line with two maxima and suggests the presence of two critical points.

We analyze in detail this potential with MD. In agreement with the previous results for potentials with a short range attraction [39], we show that the phase diagram has no stable liquid phase. Studying the metastable liquid phase, we show that the system has a low density liquid (LDL) and a high density liquid (HDL) with two fluid-fluid transitions in the supercooled phase. The low- ρ transition ends in a gas-LDL critical point C_1 and the

high- ρ transition ends in a gas-HDL critical point C_2 .

The comparison of MD results with HNC results is

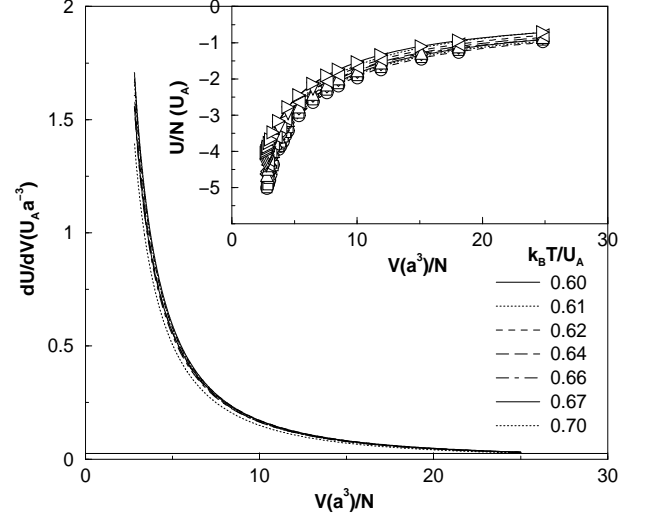


FIG. 15: The derivative $(\partial U/\partial V)_T$ calculated by using the cubic expression in Fig. 14 with the parameters in Tab. I as function of the specific volume V/N for temperatures (top to bottom) $k_B T/U_A = 0.60, 0.61, 0.63, 0.64, 0.66, 0.67, 0.7$. The derivative, in the considered range of V/N , is always larger than $0.025U_A/a^3$ (bottom horizontal line). Inset: The same MD results in Fig. 14 for U/N plotted as a function of V/N . The symbols are the same as in Fig. 14.

reasonable and, surprisingly, is better at intermediate ρ than at low ρ , confirming that, at low ρ , the HNC underestimates the effect of the attractive interaction and overestimates the effect of the repulsive interaction.

We address the question of whether the presence of two fluid-fluid critical points implies the presence of the density anomaly. By explicit calculation, we show that the condition for the density anomaly is never satisfied in the range of T and V considered here. Our results suggest that the density anomaly is always ruled out for this choice of potential parameters, showing that the possibility of a system with a second critical point is not necessarily restricted to liquids with an anomalous behavior of the density. Due to the relevance of soft-core potentials in protein solutions, colloids, melts and pure systems, like liquid metals, this result opens a new direction in the search for a liquid-liquid critical point.

VIII. ACKNOWLEDGEMENTS

We wish to thank M. C. Barbosa, P. V. Giaquinta, S. Mossa, G. Pellicane, A. Scala, F. W. Starr and especially F. Sciortino for helpful suggestions and for interesting and stimulating discussions. We thank NSF Chemistry Division (CHE-0096892) for support.

-
- [1] P.G. Debenedetti, *Metastable Liquids: Concepts and Principles* (Princeton Univ. Press, Princeton, 1998). M.-C. Bellissent-Funel ed., *Hydration Processes in Biology. Theoretical and Experimental Approaches*, NATO ASI Series A, vol.305 (IOS Press, Amsterdam, 1998). G.W. Robinson, S. Singh, S.-B. Zhu, and M.W. Evans, *Water in Biology, Chemistry and Physics* (World Scientific, Singapore, 1996).
- [2] P.C. Hemmer and G. Stell, Phys. Rev. Lett. **24**, 1284 (1970); G. Stell and P.C. Hemmer J. Chem. Phys. **56**, 4274 (1972); P.T. Cummings and G. Stell, Mol. Phys. **43**, 1267 (1981); E. Velasco, L. Mederos, G. Navascués, P.C. Hemmer, P.C., and G. Stell, Phys. Rev. Lett. **85**, 122 (2000); R. I. Beecroft and C. A. Swenson, Journal of Physical Chemistry Sol. **15**, 234 (1960); J. M. Kincaid, G. Stell, and C. K. Hall, J. Chem. Phys. **65**, 2161 (1976); J. M. Kincaid, G. Stell, and E. Goldmark, *ibid.* **65**, 2172 (1976); J. M. Kincaid and G. Stell, *ibid.* **67**, 420 (1977); C. K. Hall and G. Stell, Phys. Rev. A **7**, 1679 (1973).
- [3] M. Silbert and W.H. Young, Phys. Lett. **58A**, 469 (1976); D. Levesque and J.J. Weis, *ibid.* **60A**, 473 (1977); J.M. Kincaid and G. Stell, *ibid.* **65A**, 131 (1978); J.M. Kincaid, G. Stell and C.K. Hall, J.Chem. Phys. **65**, 2161 (1976); J.M. Kincaid, G. Stell and E. Goldmark, *ibid.* **65**, 2172 (1976); A. Voronel, I. Paperno, S. Rabinovich, and E. Lapina, Phys. Rev. Lett. **50**, 247–249 (1983).
- [4] See for example W.M. Shyu, J.H. Wehling, and M.R. Cordes, Phys. Rev. B **4**, 1802 (1971); M. Appapillai and V. Heine, Technical Report No. 5 of Theory of Condensed Matter Group, Cavendish Laboratory, Cambridge (1972); K.K. Mon, M.W. Ashcroft, and G.V. Chester, Phys. Rev. B **19**, 5103 (1979); G. Kahl and J. Hafner, Solid State Commun. **49**, 1125 (1984).
- [5] J.M. Lawrence, M.C. Croft, and R.D. Parks, Phys. Rev. Lett. **35**, 289 (1975).
- [6] See for example S.H. Behrens, D.I. Christl, R. Emmerzael, P. Schurtenberger, and M. Borkovec, Langmuir **16**, 2566 (2000); D. Wei and G.N. Patey, Phys. Rev. Lett. **68**, 2043 (1992); Phys. Rev. A **46**, 7783 (1992).
- [7] P.G. Debenedetti, V.S. Raghavan, and S.S. Borick, J. Phys. Chem. **95**, 4540 (1991).
- [8] F.H. Stillinger and T. Head-Gordon, Phys. Rev. E **47**, 2484 (1993); F.H. Stillinger and D.K. Stillinger, Physica A **244**, 358 (1997); T. Head-Gordon and F. H. Stillinger, J. Chem. Phys. **98**, 3313 (1993).
- [9] M. R. Sadr-Lahijany, A. Scala, S. V. Buldyrev, and H. E. Stanley, Phys. Rev. Lett. **81**, 4895 (1998); Phys. Rev. E **60**, 6714 (1999); A. Scala, M. R. Sadr-Lahijany, N. Giovambattista, S. V. Buldyrev, H. E. Stanley, *ibid.* **63**, 041202 (2001); J. Stat. Phys. **100**, 97–106 (2000).
- [10] G. Franzese, G. Malescio, A. Skibinsky, S.V. Bulderev, H.E. Stanley, Nature **409**, 692 (2001).
- [11] G. Malescio and G. Pellicane, Phys. Rev. E **63**, 020501 (2001).
- [12] E.A. Jagla, Phys. Rev. E **58**, 1478 (1998); J. Chem. Phys. **111**, 8980 (1999); Phys. Rev. E **63**, 061501 (2001); *ibid.* **63**, 061509 (2001).
- [13] J.P. Hansen and I.R. McDonald, *Theory of simple liquids* (Academic Press, London, 1976).
- [14] D. Frenkel and B. Smit, *Understanding molecular simulation : from algorithms to applications* (Academic Press, San Diego, 1996); M.P. Allen and D.J. Tildesley, *Computer Simulation of Liquids* (Oxford University Press, New York, 1989).
- [15] Y. Katayama, T. Mizutani, W. Utsumi, O. Shimomura, M. Yamakata, K. Funakoshi, Nature **403**, 170 (2000); S. Falconi, M. Nardone, G. Monaco, W. Crichton, private communication.
- [16] T. Morishita, Phys. Rev. Lett. **87**, 105701 (2001).
- [17] P.H. Poole, F. Sciortino, U. Essmann, and H.E. Stanley, Nature **360**, 324 (1992) and Phys. Rev. E **48**, 3799 (1993); H.E. Stanley, C.A. Angell, U. Essmann, M. Hemmati, P.H. Poole, and F. Sciortino, Physica A **206**, 122 (1994); F. Sciortino, P.H. Poole, U. Essmann, and H.E. Stanley, Phys. Rev. E **55**, 727 (1997); P.H. Poole, F. Sciortino, T. Grande, H.E. Stanley, and C.A. Angell, Phys. Rev. Lett. **73**, 1632 (1994); S. Harrington, R. Zhang, P.H. Poole, F. Sciortino, H.E. Stanley, *ibid.* **78**, 2409 (1997); P.H. Poole, T. Grande, C.A. Angell, P.F. McMillan, Science **275**, 322 (1997); M. Canpolat, F. W. Starr, A. Scala, M. R. Sadr-Lahijany, O. Mishima, S. Havlin and H. E. Stanley, Chem. Phys. Lett. **294**, 9-12 (1998).
- [18] E.G. Ponyatovskii, V.V. Sinitsyn, and T.A. Pozdnyakova, JETP Lett. **60**, 360 (1994); H. Tanaka, Nature **380**, 328 (1996) and J. Chem. Phys. **105**, 5099 (1996); C.T. Moynihan, Mater. Res. Soc. Symp. Proc. **455**, 411 (1997); C.A. Jeffery and P.H. Austin, J. Chem. Phys. **110**, 484 (1999).
- [19] M. van Thiel and F.H. Ree Phys. Rev. B **48**, 3591 (1993).
- [20] J.N. Glosli and F.H. Ree, Phys. Rev. Lett. **82**, 4659 (1999).
- [21] D.J. Lacks, Phys. Rev. Lett. **84**, 4629 (2000).
- [22] I. Saika-Voivod, F. Sciortino, and P.H. Poole, Phys. Rev. E **63**, 011202 (2001); I. Saika-Voivod, P.H. Poole, F. Sciortino, Nature **412**, 514 (2001).
- [23] S. Sastry, in *Liquid-Liquid Phase Transition Phenomena* NATO Advanced Research Workshop, Volga River, V. Brazhkin, S. V. Buldyrev, V. Ryzhov, and H. E. Stanley eds., (Kluwer, Dordrecht, 2001).
- [24] O. Mishima and H.E. Stanley, Nature **396**, 329 (1998); *ibid.* **392**, 164 (1998); O. Mishima, Phys. Rev. Lett. **85**, 334 (2000).
- [25] M.-C. Bellissent-Funel, Europhys. Lett. **42**, 161 (1998); Nuovo Cimento **20D**, 2107-2122 (1998).
- [26] A.K. Soper and M.A. Ricci, Phys. Rev. Lett. **84**, 2881 (2000).
- [27] V.V. Brazhkin, E.L. Gromnitskaya, O.V. Stalgorova, and A.G. Lyapin, Rev. High Pressure Sci. Tech. **7**, 1129 (1998); V.V. Brazhkin, S.V. Popova, and R.N. Voloshin, High Pressure Res. **15**, 267 (1997).
- [28] M.C. Wilding, P.F. McMillan, and A. Navrotsky J. Non-cryst. Solids (in press).
- [29] These diagrams are called bridge diagrams [13].
- [30] J.M.J. Van Leeuwen, J. Groenvelt and J.De Boer, Physica **25**, 792 (1959); G.S. Rushbrooke, *ibid.* **28**, 259 (1960); E. Meeron, J. Math. Phys. **1**, 192 (1960); T. Morita, Prog. Theor. Phys. **23**, 829 (1960); L. Verlet, Il Nuovo Cimento, **18**, 77 (1960).
- [31] See C. Caccamo, Phys. Rep. **274**, 1 (1996) and references therein.
- [32] P.D. Poll and N.W. Ashcroft, Phys. Rev. A **35**, 5167

- (1987).
- [33] The equations of state can be obtained following three different routes [13]: by thermodynamic integration of K_T , by using the Clausius virial theorem, or by integration of the Maxwell relations between P , entropy and total energy. As already known [13], due to the approximate nature of the HNC closure, the results of the three different routes do not coincide, i.e. the theory is thermodynamically inconsistent. The inconsistency can be partially removed by modifying the closure in such a way that it depends on a parameter. This parameter is usually fixed by requiring that the virial pressure is equal to the pressure calculated through the compressibility route. In this way a more accurate estimate of the spinodal line is obtained and, due to the thermodynamic consistency, also the binodal (or coexistence) line can be calculated. However the numerical procedures becomes much more computational-time consuming than the solution of the HNC equations without the thermodynamic consistency. Therefore, for a first extensive investigation in the parameter space of the model potential, we choose to solve the integral equations in the HNC approximation without imposing the thermodynamic consistency.
- [34] The overall shape of the instability line with two local maxima is consistent with the phase diagram derived by C.F. Tejero and M. Baus, Phys. Rev. E **57**, 4821 (1998) within a van der Waals approach for an effective density-dependent interaction potential.
- [35] D.C. Rapaport, *The art of molecular dynamics simulation* (Cambridge University Press, Cambridge, 1995).
- [36] H.J.C. Berendsen, J.P.M. Postma, W.F. van Gunsteren, A. Di Nola, and J.R. Haak, J. Chem. Phys. **81**, 3684 (1984).
- [37] It is known that in finite-systems a first-order transition give rise to a transition region rather than a transition line (well defined only in the thermodynamic limit) [14].
- [38] The present estimates are fully consistent with those in Ref.[10] but slightly different as consequence of the calculation of new data points.
- [39] M.H.J. Hagen, E.J. Meijer, G.C.A.M. Mooij, D. Frenkel, H.N.W. Lekkerkerker, Nature **365**, 425 (1993); C.F. Tejero, A. Daanoun, H.N.W. Lekkerkerker, and M. Baus, Phys. Rev. Lett. **73**, 752 (1994); P. Rein ten Wolde and D. Frenkel, Science **277**, 1975 (1997).
- [40] G.C.A.M. Mooij, D. Frenkel, and H.N.W. Lekkerkerker, Nature **365**, 425 (1993); P. Bolhuis and D. Frenkel, Phys. Rev. Lett. **72**, 2211 (1994).
- [41] S.S. Borick, P.G. Debenedetti, and S. Sastry, J. Phys. Chem. **99**, 3781 (1995); T.M. Truskett, P.G. Debenedetti, S. Sastry, and S. Torquato, J. Chem. Phys. **111**, 2647 (1999); J.R. Errington and P.G. Debenedetti, Nature **409**, 318 (2001).
- [42] N. Guisani and V.B. Henriques, J. Chem. Phys. **115**, 5238 (2001).

TABLE I: Parameters for the cubic fit $U/N = a_0 + a_1\rho + a_2\rho^2 + a_3\rho^3$ of the MD calculations for the energy density U/N in Fig. 14 for different temperatures. The errors on the fitting parameters are on the last decimal digit.

$k_B T/U_A$	a_0	a_1	a_2	a_3
0.60	-0.2309	-20.46	39.64	-56.90
0.61	-0.2228	-19.74	36.52	-51.11
0.63	-0.1279	-21.38	49.64	-76.71
0.64	-0.1098	-20.24	44.19	-65.17
0.66	-0.0458	-20.48	48.08	-70.72
0.67	-0.0733	-21.50	52.43	-75.20
0.70	-0.0446	-18.18	37.39	-49.14